Tunable hexagonal boron nitride topological optical delay line in the visible region

Hongming Fei (费宏明)[1*], Min Wu (武 敏)[2], Han Lin (林 瀚)[3**], Yibiao Yang (杨毅彪)[4], and Liantuan Xiao (肖连团)[1***]

[1] College of Physics, Taiyuan University of Technology, Taiyuan 030024, China

[2] College of Information Engineering, Shanxi Vocational University of Engineering Science and Technology, Jinzhong 030619, China

[3] College of Science, RMIT University, Melbourne, Victoria 3000, Australia

[4] College of Electronic Information and Optical Engineering, Taiyuan University of Technology, Taiyuan 030024, China

*Corresponding author: feihongming@tyut.edu.cn
**Corresponding author: han.lin2@rmit.edu.au
***Corresponding author: xiaoliantuan@tyut.edu.cn

Tunability, ultracompact design, high group index, low loss, and broad bandwidth are desired properties for integrated optical delay lines (ODLs). However, those properties are challenging to achieve simultaneously in the visible region. This paper proposes a tunable hexagonal boron nitride topological optical delay line (ODL) in the visible region based on valley photonic crystals. The topological edge state from the beard-type boundary allows the achievement of an ultralow group velocity close to zero, which results in a large group index of 629 at 645 nm. Moreover, we demonstrate tuning of the slow-light wavelength and optical delay times with electrically tunable liquid crystals by applying external voltage. The device has an ultracompact size of 5 μm × 2.7 μm with an optical delay distance of 25a (a is the lattice constant) and a delay time of 12 ps. Our design can provide a new possibility for designing ODLs working in the visible region for optical communication and quantum computing systems.

Keywords: valley photonic crystal; topological edge states; optical delay lines.
DOI: 10.3788/COL202422.053602

1. Introduction

Nanophotonics devices with slow-light properties can be applied to optical nonlinearity, optical switching, pulse delay, quantum optics, optical storage, and optical gain[1,2]. Furthermore, slow light can promote strong light–matter interaction, which offers possibilities for miniaturization and improvement of photonic devices. Optical delay lines (ODLs) are slow-light devices that can delay and temporarily store photons sufficiently long to enable quantum operations for optical buffering[3−10]. Integratable quantum optical chips impose higher requirements on ODLs, such as tunability, ultracompactness, low loss (high transmittance), and broad bandwidth. One of the key parameters of an ODL is the delay time (t), depending on the optical path length (L) and the group velocity (v_g) in the relationship of $t = L/v_g$. In general, a long delay time is preferred, which can be achieved by either enlarging L or reducing v_g. Conventional ODL designs, such as microring resonators[3,4], gratings[5,6], and switchable and reconfigurable array delay lines[7−9], rely on increasing L without tuning v_g. As a result, those designs usually have millimeter sizes and are unsuitable for on-chip integration. In contrast, the slow-light effect of photonic crystals (PCs) can achieve compact ODLs[10-20] for high-density integration by reducing v_g, including modified PC waveguides[10], PC coupled optical waveguides[11] based on PC cavities, and PC microrings[12]. So far, all the ODLs based on PC structures work in the telecommunication wavelength range because a complete photonic bandgap is generally required to achieve high transmission efficiency, requiring high refractive index materials (e.g., silicon). However, there are few high refractive index materials with low absorption in the visible region, and it is challenging to achieve a complete photonic bandgap in conventional PCs using low refractive index materials. There is no demonstration of PC-based ODLs working at visible wavelengths. In addition, the backward scattering of PC-based ODLs introduces high insertion loss, especially near the slow-light region, limiting the application of PC-based slow-light devices[21,22]. Therefore, the design of PC-based ODLs with antibackscattering capability is particularly critical.

The topological edge states of valley photonic crystals (VPCs) allow robust unidirectional transmission of circularly polarized light without backscattering introduced by structural

defects[15–21,23–29]. Slow-light waveguides based on VPCs have been demonstrated in different wavelength regions, including the near-infrared (900 nm)[15–19], telecommunication (1500 nm)[16], and gigahertz regimes[19]. Furthermore, slow-light waveguides based on VPCs can work with embedded quantum emitters, which can be used to realize a chiral quantum interface[27,28]. The quantum dot emission coupled to slow-light modes with a high group index of over 20 around 900 nm has been reported[18]. Compared with conventional PC-based slow-light devices, VPC-based designs have the advantages of long delay time and low loss. However, there is no demonstration of VPC-based slow-light devices in the visible wavelength region.

In our previous works, we have demonstrated the possibility of achieving VPCs working in the visible region[30–33] based on two-dimensional (2D) hexagonal boron nitride (hBN) materials[30–41], which can support topological edge states. 2D hBN exhibits the properties of an ultrabright quantum single-photon source in the visible wavelength band[36,37], which shows great potential for realizing quantum optics chips in the visible range based on topological photonics. It is meaningful to design VPC devices based on 2D hBN materials, which can directly integrate and couple the on-chip quantum light sources from hBN for quantum computing and information processing[39,41]. One of the scenarios could be enhancing the single-photon interaction with material by coupling the quantum emitter into VPC devices based on 2D hBN material. More importantly, hBN is able to generate ultrabright single-photon emitters on a chip by using

a focused ion beam (FIB) to introduce defects at desired locations, which can be coupled into the designed VPC TODL for future study[36]. This paper presents the first ODL design based on an hBN VPC structure in the visible region. The unique property of the topological edge stages of the beard-type boundary shows an ultralow group velocity of 0.0016c (c is the velocity of light), corresponding to a high group index of 629. The device has an ultracompact size of 5 μm × 2.7 μm with an optical delay distance of 25a (a is the lattice constant) and a delay time of 12 ps. In addition, the working wavelength can be tuned by applying external voltages with electrically tunable liquid crystals filled in the air holes. This design provides a new idea for developing quantum optics devices based on topological photonics for quantum communication and information processing[42].

2. Results

2.1. Conceptual design of hBN VPC

The conceptual design of the ODL in the visible range is shown in Fig. 1(a), in which the topological edge states have an ultralow group velocity corresponding to a short effective wavelength. The VPC structure is designed in two steps. (1) A honeycomb photonic crystal structure (circular air holes embedded in a 220 nm thick freestanding hBN substrate) with C_{6v} symmetry is designed to achieve a Dirac point in the photonic band.
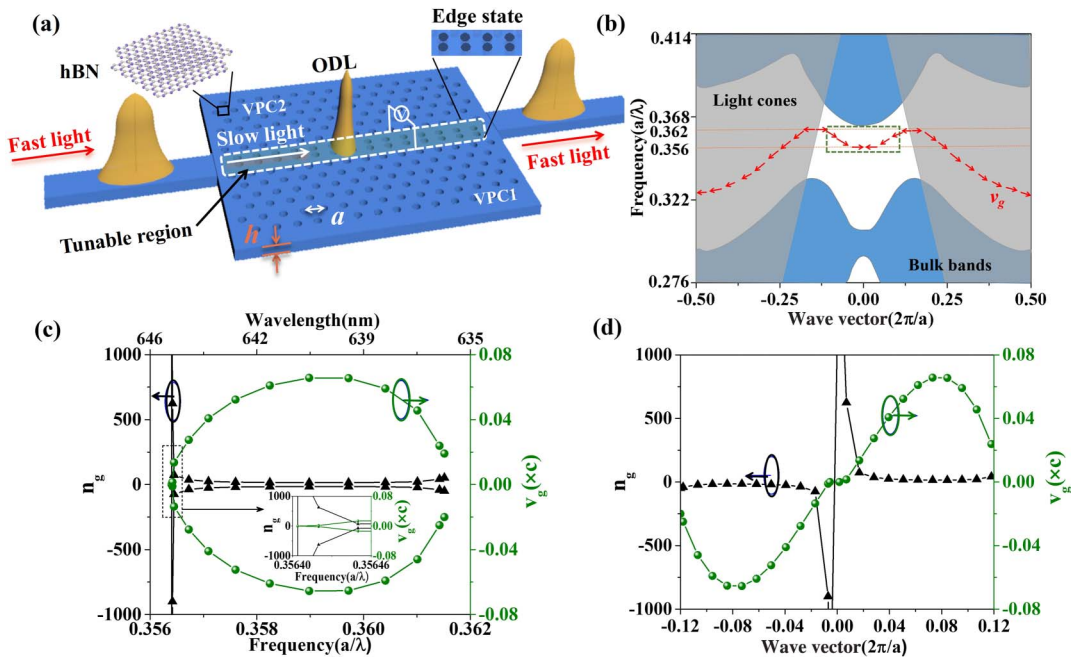

Fig. 1. (a) The schematic diagram of an ODL based on a VPC structure, in which the yellow shadow marks the slow-light waveguide. The red arrows mark the propagation direction of incident light. As the incident light couples into the slow-light waveguide, the effective wavelength is shortened, resulting in a slow group velocity. The inset shows the molecular structure of hBN material. (b) The band diagram of the beard-type boundary. The blue area is the bulk band, and the gray area is the light cone. The two red arrows mark the directions of the v_g. (c) The group index (n_g) and the group velocity (v_g) plots versus wavelength (λ) and frequency. (d) The group index (n_g) and the group velocity (v_g) plots versus wave vector (k).

(2) The C_{6v} symmetry of the structure is changed to C_3 symmetry by changing the size of the air holes, which degenerates the Dirac points at the K and K' valleys (see Supplementary Material, Section 1) to create a topological photonic bandgap. Previous studies have demonstrated that a triangular lattice with C_3 symmetry can generate topologically protected edge states and still support topological edge modes in a wide bandgap[43,44]. In this work, the ODL structure comprises two VPCs with a lattice constant of $a = 230$ nm, namely, VPC1 and VPC2 (mirror symmetrical about the x axis) [Fig. 1(a)]. The photonic band diagram and the transmission of transverse electric (TE)-polarized modes are calculated using commercial software (Lumerical FDTD) based on the finite-difference time-domain (FDTD) method. 2D hBN has a layered structure, and the overall thickness depends on the number of layers. The layered structure results in an anisotropic refractive index ($n_x = n_y \neq n_z$, n_x, n_y are the in-plane refractive indices, n_z is the out-of-plane refractive index)[32], which is considered in the calculation. To achieve the largest bandgap, the radius of the small air holes is $R_2 = 0$; meanwhile, the radius of the large air holes is $R_1 = 60$ nm. The bandgap is in the range of 0.345–0.362a/λ, corresponding to the wavelength range of 635.5 to 667 nm, which defines the maximum working bandwidth. The 2D Brillouin zone has periodic boundary conditions and is also a closed surface with the same topological properties as the ring surface, satisfying the Berry phase $\gamma_n(\boldsymbol{k}) = \oint d\boldsymbol{k} \cdot A_n(\boldsymbol{k})$ requirement for the closed loop condition, where $A_n(\boldsymbol{k})$ is the Berry connection. According to the bulk-boundary correspondence[26], when the topological number at the interface changes, a topological phase transition occurs. Moreover, the topological property of VPC1 and VPC2 can be described by the valley-dependent topological index $C_{\tau_z} = \frac{\tau_z \mathrm{sgn}(\lambda_{\varepsilon_r}^P)}{2}$[45], which are $C_K = \frac{1}{2}$ and $C_{K'} = -\frac{1}{2}$ for K and K' valleys, respectively. Therefore, even though the total Chern number is equal to zero, we can define this new nonzero topological invariant, namely, the valley Chern number, $C_V = C_K - C_{K'}$, which is a well-defined topological number protected by time-reversal symmetry[46]. As a result, the valley Chern numbers of VPC1 and VPC2 are +1 and −1, respectively. The opposite valley Chern numbers are also necessary to generate topological edge states at the boundary between VPC1 and VPC2.

The VPC1 and VPC2 with different topological properties can be combined into two types of valley interface waveguides: mirror-symmetric beard-type and staggered-symmetric zigzag-type, supporting different edge states (see Supplementary Material, Section 2). The group velocity of the edge states is $v_g = d\omega/dk$, where ω and k are the angular frequency and the wave vector, respectively[10]. Therefore, to achieve the slow-light effect, v_g should be as low as possible, translating into a small slope in the dispersion diagram. A v_g close to 0 can be achieved at the peak or dip (the slope is near 0) of the edge state. As shown in Fig. S2(d) (Supplementary Material, Section 2), there is no peak or dip in the edge state plot of the zigzag-type boundary. Thus, it is challenging to achieve a low v_g in this case. In

comparison, due to the mirror-symmetric shape of the beard-type boundary, the minimum is achieved at the center ($k = 0$) (see Supplementary Material, Section 2), which corresponds to $v_g = 0$ theoretically. Therefore, it is possible to form a standing wave with zero group velocity at the point [Fig. 1(b)], which still retains the topological properties, thus forming a standing wave that can be useful for exciting nonlinearity with low power[15,16]. In addition, the v_g around that point all shows a small value, which confirms the achievement of the slow-light effect. Therefore, the beard-type boundary is chosen in this study for designing ODLs. The edge-state dispersion curves of the beard-type boundary are shown in Fig. 1(b); the red arrows represent the orientation of the tangent line (group velocity direction) at each position of the dispersion curve. The tangent line of the dispersion curve at $k = 0$ and $k = \pm 0.14(2\pi/a)$ (corresponding to the minimum and maximum of the v_g in the edge state plot) points to the horizontal direction, meaning the v_g is 0.

The group index n_g is defined as $n_g = c/v_g$, where c is the speed of light. The plots of n_g and v_g depending on the wavelength (λ) and wave vector (k) are shown in Figs. 1(c) and 1(d), respectively. It can be seen that an ultralow group velocity (0.0016c) can be achieved near $k = 0$ [Fig. 1(d)] around the minimum of the edge state curve [Fig. 1(b)], which corresponds to a high group index of $n_g = 629$. This is relatively high compared to other types of PC slow-light waveguides[10,14,18], which can be attributed to the unique dispersion properties of the edge state of the beard-type boundary. The working wavelength of the slow-light waveguide can be controlled by the geometric structure of the boundary or the refractive index contrast, which is 645 nm for the current design. Theoretically, the n_g can become infinitely large at $k = 0$ or $k = \pm 0.14(2\pi/a)$; however, backscattering at large n_g affects the light transmission, limited by localization effects and light loss due to defects[10]. So in the actual slow-light device design, we choose the working wavelength slightly off the $k = 0$ point instead of at the point. On the other hand, the increase of n_g is inevitably accompanied by an undesirable narrower operational bandwidth for any slow-light waveguide design[12]. Therefore, the normalized delay-bandwidth product (NDBP) is introduced, defined as DBP= $n_g \Delta\omega/\omega_0$[13], where $\Delta\omega/\omega_0$ is the normalized bandwidth of a slow-light region and ω_0 is the central frequency of the normalized bandwidth. The NDBP of our design is 0.22 from 637 to 644 nm, calculated from Fig. 1(c), which is suitable for most applications[12]. The group velocity dispersion (GVD) parameter β_2, which affects the distortion of short optical pulse is expressed by the second-order derivative of the dispersion relation[47]: $\beta_2 = \frac{d^2 k}{d\omega^2} = -(\frac{1}{v_g})^3 \frac{d^2\omega}{dk^2} = \frac{1}{c}\frac{dn_g}{d\omega}$. The order of GVD is 230 s^2/m for this range of frequency; the details are shown in the Supplementary Material, Section 3.

In order to study the transmission of the edge state, we plot the Poynting vector [Fig. 2(a)] and the electric and magnetic intensity distributions [Figs. 2(b) and 2(c)] of the edge state in the VPC waveguide. The incident light is a right-handed circularly polarized (RCP) light. Based on the spin-valley locking
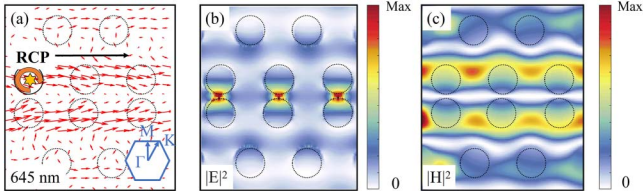
Fig. 2. (a) Poynting vector distributions at 645 nm. (b) and (c) Edge state's electric and magnetic field intensity distributions at 645 nm.

effect, the left-handed circularly polarized (LCP) light and RCP light show identical transmittance spectra (see Supplementary Material, Section 4). The Poynting vector indicates the energy flow direction of the electromagnetic field, which is defined as $\vec{S} = \vec{E} \times \vec{H}$. The direction of each Poynting vector is determined by the slope of the curve, which also points to the direction of the group velocity. It can be seen that the Poynting vectors at the wavelength of 645 nm are along the path in the beard-type boundary [Fig. 2(a)], confirming the unidirectional propagation property of the edge state. In addition, in the middle, between the two rows of air holes, the horizontal component of the Poynting vectors is relatively small, corresponding to low group velocity. Meanwhile, the electric field intensity distribution shows a near-standing wave distribution [Fig. 2(b)]. A similar effect can also be identified in the magnetic field intensity distributions, as shown in Fig. 2(c).

2.2. Tunable edge state in the slow-light waveguide

The working wavelength of the edge state can be controlled by the geometric structure of the boundary or the refractive index contrast, which serves to tune the slow-light frequency. First, the slow-light frequency can be tuned by changing the radius of the air holes at the boundary (see Supplementary Material, Section 5). When reducing the radius of the holes (from 60 to 54 nm), the slow-light wavelength redshifts from $0.353a/\lambda$ to $0.356a/\lambda$ (646 to 650 nm) (see Supplementary Material, Section 5) due to the increase of the effective refractive index. Meanwhile, we tuned the refractive indices of the holes at the boundary by filling different materials [including water ($n = 1.33$) and oil ($n = 1.5$)] and simulated the dispersion curves of the edge states for comparison (see Supplementary Material, Section 5). The results show that as the refractive index of holes at the boundary increases, the slow-light wavelength of maximum n_g (minimum v_g) redshifts from $0.344a/\lambda$ to $0.356a/\lambda$ (646 to 669 nm), thus confirming the feasibility of tuning the working wavelength of the slow-light waveguide. In addition, if an electrically tunable material (e.g., liquid crystal) is applied in the holes, it is possible to apply external voltage to tune the working wavelength. At room temperature, the ordinary (n_o) and extraordinary (n_e) refractive indices of liquid crystal E7 are 1.51 and 1.73, respectively, which were measured by the multiwavelength Abbe refractometer[48]. With an increasing voltage, n_e decreases and gradually approaches n_o[49,50]. As a result, the birefringence of the liquid crystal tends to decrease with the
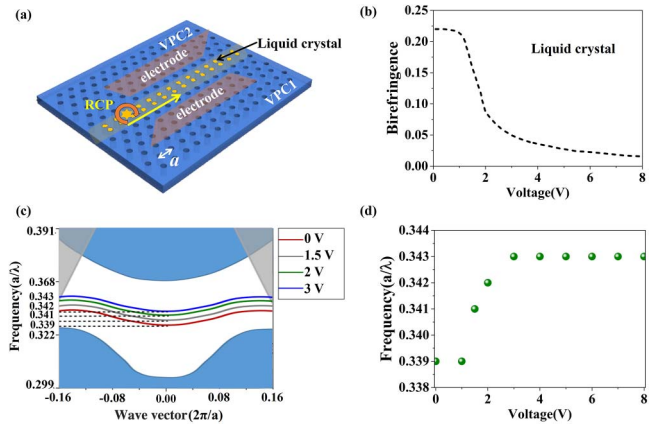

Fig. 3. (a) Schematic diagram of beard-type boundary filled with liquid crystal, where the yellow columns indicate tunable regions; (b) birefringence plot of liquid crystal at different voltages[49]; (c) edge state plots at different voltages; (d) plot of slow-light wavelengths at different voltages.

voltage increase within a certain range [Fig. 3(b)]. The working wavelength blueshifts from $0.339a/\lambda$ to $0.343a/\lambda$ (678 to 670 nm) when the voltage increases from 0 to 8 V [Fig. 3(d)]. In addition, it is found that the slow-light wavelength stays at around $0.343a/\lambda$ when the voltage increases to more than 3 V. Therefore, the working voltage can be limited to 0–3 V; the edge states are plotted in Fig. 3(c).

2.3. Transmission properties of the ODL

The slow-light waveguide can achieve high transmittance due to the unique topological edge states in VPCs. Meanwhile, the delay time can be controlled by the length (L) of the waveguides in different types, such as Z-type and Ω-type waveguides, respectively. The corresponding electric field intensity distributions at the wavelength of 645 nm and the forward transmittance spectra are shown in Fig. 4. Here, RCP light is used as the light source. From the field intensity distributions in Figs. 4(a), 4(e), and 4(f), it can be seen that the RCP light can achieve a high transmittance at the working wavelength (645 nm). The straight waveguide [Fig. 4(a)] has an overall transmittance higher than -0.969 dB (0.8) in the bandwidth from 635 to 667 nm (32 nm), and the highest transmittance is -0.457 dB (0.9) at 645 nm. The gray region represents the unidirectional transmission working bandwidth, where the forward transmittance is higher than -2.5 dB (0.56) in Fig. 4. The bandwidth of the straight waveguide decreases as the refractive index of the edge-state structure increases in Figs. 4(b)–4(d). The refractive index of the hBN slab in this paper is also low ($n < 2.35$), which also contributes to the relatively high loss. The maximal working bandwidth of the waveguides depends on the width of the bandgap and the geometry of the waveguide (see Supplementary Material, Section 4). In addition, both Z-type and Ω-type waveguides have bandwidths from 635 to 650 nm (15 nm) and can still reach the transmittance more than -1.24 dB (0.75) at 645 nm despite a decrease in overall
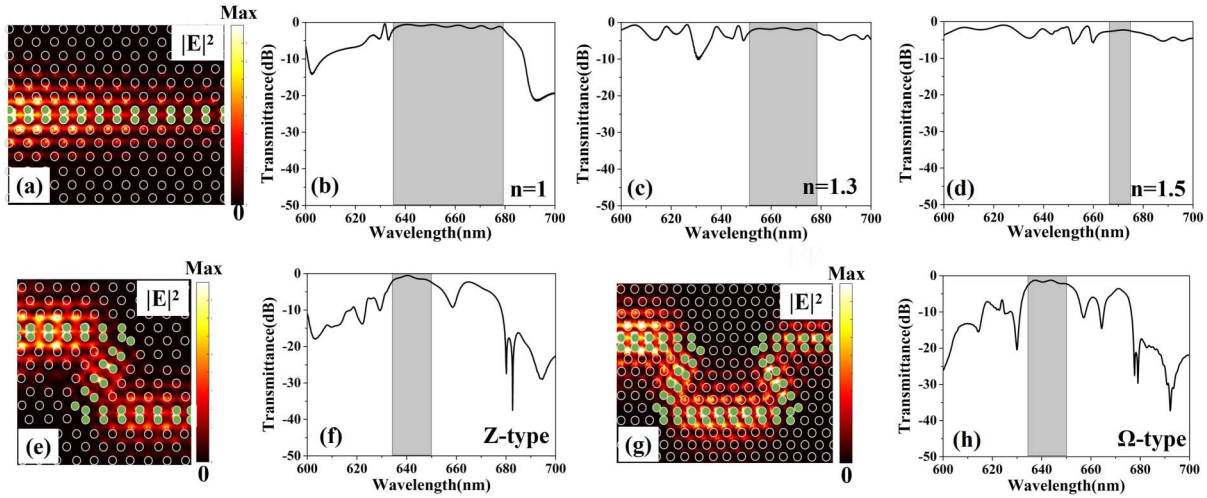
Fig. 4. (a) Electric field intensity distributions in a straight waveguide at 645 nm; (b)–(d) transmittance spectra of the straight waveguides with different refractive indices; the gray shadow marks the working bandwidth; electric field intensity distributions at 645 nm and transmittance spectra of Z-type [(e) and (f)] and Ω-type waveguides [(g) and (h)]; the gray region represents the unidirectional transmission working bandwidth, where the forward transmittance is higher than −2.5 dB.

transmittance. Therefore, the Z-type and Ω-type designs are beneficial for achieving long ODLs while ensuring that the designed waveguide maintains high transmission and small footprints, which is essential for on-chip integration.

The slow-light waveguide can be directly applied as an ODL for temporarily storing photons, providing a new approach to the buffer in photonic chips. The optical delay time is obtained from the calculated group velocity as $\Delta t = L/v_g$, where Δt is the delay time, and L is the optical path length of an ODL. The straight waveguide with a total length of $L = 8.5a$ (2 µm) can achieve a delay time Δt of 4 ps at the wavelength of 645 nm. The device has a size of 4.5 µm × 2.5 µm. By increasing the optical path length to $L = 17a$ (3.9 µm), the Z-type waveguide can obtain a delay time of 8 ps at 645 nm; the device size is 4.5 µm × 3.5 µm. Furthermore, the Ω-type waveguide has $L = 25a$ (5.75 µm) with a structure size of 5 µm × 2.7 µm, showing a delay time of 12 ps. Figure 5(a) shows that the refractive index tuning allows tuning the required delay time at different wavelengths. As the long delay time can be achieved at the minimum of the edge state (slow-light wavelength), increasing the refractive index of the holes can redshift the slow-light wavelength. The delay times of the Ω-type waveguides filled with liquid

crystals at 667 nm (around $k = 0$ point) can be tuned from 5 to 0.18 ps, when the voltage increases from 0 to 3 V in Fig. 5(b). For the performance of these types of waveguides filled with liquid crystals at different voltages, see Supplementary Material, Section 6. In addition, we discuss the time domain analysis of the ODL based on the straight waveguide[47], and compare the performance of the proposed slow-light waveguide with a conventional PC slow-light waveguide in the Supplementary Material, Section 3. This proves that this result is the best among any slow-light waveguides in the visible region, to the best of our knowledge, which makes it suitable for most applications. The actual experiment, the potential experimental methods of hBN VPC[36], and the technique of dipping holes in liquid crystals[51] are described in the Supplementary Material, Sections 7 and 8.

3. Conclusion

This paper demonstrates an ultracompact tunable topological ODL based on hBN VPCs. By comparing the edge states of the two types of boundaries, we demonstrated that the beard-type boundary could achieve zero group velocity in theory and was suitable for designing a slow-light waveguide working as an ODL. Meanwhile, the working wavelength of the slow-light waveguide can be adjusted by the radii or the refractive indices of the holes at the boundary, which can also be electrically controlled. By designing Z-type and Ω-type waveguides, the optical path length of the waveguides can be effectively increased without compromising the ultracompact design. Those designs can achieve a delay time of up to 12 ps at the wavelength of 645 nm with high transmittance. In addition, the designed hBN VPCs can be scaled to achieve desired slow-light wavelength in the visible range of 500–700 nm. This design provides a new possibility for the development of optical quantum information storage.
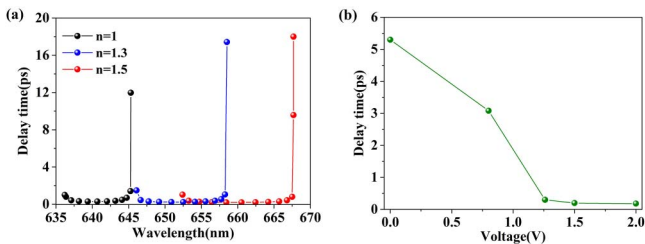

Fig. 5. (a) Optical delay times of the Ω-type waveguides with different refractive indices; (b) optical delay times of the Ω-type waveguides filled with liquid crystals at different voltages at 667 nm.

Considering conventional PC-based ODLs, achieving a high transmittance with a long optical path length in the visible region is extremely challenging because a high refractive index is generally required to achieve a complete photonic bandgap for high transmittance. However, dielectric materials working in the visible region generally have a low refractive index, which is unsuitable for achieving a complete photonic bandgap. As a result, no PC-based ODL working in the visible region has been demonstrated. Here we overcome this challenge by invoking a new design principle based on VPC, which can achieve high transmittance and long delay based on low refractive index dielectric materials. In addition, the defect-immune antiscattering propagation capability can lower experimental fabrication requirements and make the designs suitable for manufacturing by current nanofabrication techniques. Thus, our design opens new possibilities in designing ODLs, particularly in designs based on PC structures.

Acknowledgements

References

1. T. Krauss, "Why do we need slow light?" Nat. Photonics **2**, 448 (2008).
2. C. C. Lu, W. Zhao, S. Zhang, *et al.*, "Observation of topological rainbow in non-Hermitian systems," Chin. Opt. Lett. **21**, 123601 (2023).
3. W. S. Shan, L. J. Lu, X. Y. Wang, *et al.*, "Broadband continuously tunable microwave photonic delay line based on cascaded silicon microrings," Opt. Express **29**, 3375 (2021).
4. N. M. Tessema, Z. Cao, J. H. C. Van Zantvoort, *et al.*, "A tunable Si₃N₄ integrated true time delay circuit for optically-controlled K-band radio beamformer in satellite communication," J. Lightwave Technol. **34**, 4736 (2016).
5. X. Wang, W. Shi, R. Vafaei, *et al.*, "Uniform and sampled Bragg gratings in SOI strip waveguides with sidewall corrugations," IEEE Photon. Technol. Lett. **23**, 290 (2011).
6. X. Wang, Y. H. Zhao, Y. H. Ding, *et al.*, "Tunable optical delay line based on integrated grating-assisted contradirectional couplers," Photonics Res. **6**, 880 (2018).
7. Q. Q. Song, "Scalable and reconfigurable continuously tunable lithium niobate thin film delay line using graphene electrodes," IEEE Photonics J. **14**, 6648708 (2022).
8. X. Y. Wang, L. J. Zhou, R. F. Li, *et al.*, "Continuously tunable ultra-thin silicon waveguide optical delay line," Optica **4**, 507 (2017).
9. G. Arregui, J. Gomis-Bresco, C. M. Sotomayor-Torres, *et al.*, "Quantifying the robustness of topological slow light," Phys. Rev. Lett. **126**, 027403 (2021).
10. M. Momchil and V. Savona, "Wide-band slow light in compact photonic crystal coupled-cavity waveguides," Optica **2**, 631 (2015).
11. Y. D. Zhang, L. P. Wang, H. L. Fan, *et al.*, "Ultra-slow light with high normalized delay–bandwidth product and refractive-index sensing in photonic crystal coupled-cavity waveguide," Opt. Commun. **523**, 128721 (2022).
12. S. A. Schulz, L. O'Faolain, D. M. Beggs, *et al.*, "Dispersion engineered slow light in photonic crystals: a comparison," J. Opt. **12**, 104004 (2010).
13. L. Liu, Y. K. Wang, and M. X. Li, "Slow light in topological coupled-corner-state waveguide," J. Phys. D: Appl. Phys. **55**, 335104 (2022).
14. K. Hirotani, R. Shiratori, and T. Baba, "Si photonic crystal slow light waveguides optimized through informatics technology," Opt. Lett. **46**, 4422 (2021).
15. J. F. Chen, W. Y. Liang, and Z. Y. Li, "Strong coupling of topological edge states enabling group-dispersionless slow light in magneto-optical photonic crystals," Phys. Rev. B **99**, 014103 (2019).
16. H. Yoshimi, T. Yamaguchi, Y. Ota, *et al.*, "Slow light waveguides in topological valley photonic crystals," Opt. Lett. **45**, 2648 (2020).
17. H. Yoshimi, T. Yamaguchi, R. Katsumi, *et al.*, "Experimental demonstration of topological slow light waveguides in valley photonic crystals," Opt. Express **29**, 13441 (2021).
18. K. Kuruma, H. Yoshimi, Y. Ota, *et al.*, "Topologically-protected single-photon sources with topological slow light photonic crystal waveguides," Laser Photonics Rev. **16**, 2200077 (2021).
19. K. Lai, T. Ma, X. Bo, *et al.*, "Experimental realization of a reflections-free compact delay line based on a photonic topological insulator," Sci. Rep. **6**, 28453 (2016).
20. W. Zheng, L. Liu, and Y. K. Wang, "Zero-GVD slow light of coupled topological edge states in a sandwiched photonic crystal waveguide," Opt. Mater. Express **12**, 4252 (2022).
21. S. A. Mann and A. Alù, "Broadband topological slow light through Brillouin zone winding," Phys. Rev. Lett. **127**, 123601 (2021).
22. L. O'Faolain, S. A. Schulz, D. M. Beggs, *et al.*, "Loss engineered slow light waveguides," Opt. Express **18**, 27627 (2010).
23. S. Peng, N. J. Schilder, X. Ni, *et al.*, "Probing the band structure of topological silicon photonic lattices in the visible spectrum," Phys. Rev. Lett. **122**, 117401 (2019).
24. M. I. Shalaev, W. Walasik, A. Tsukernik, *et al.*, "Robust topologically protected transport in photonic crystals at telecommunication wavelengths," Nat. Nanotechnol. **14**, 31 (2019).
25. X. T. He, E. T. Liang, J. J. Yuan, *et al.*, "A silicon-on-insulator slab for topological valley transport," Nat. Commun. **10**, 872 (2019).
26. M. Ezawa, "Topological Kirchhoff law and bulk-edge correspondence for valley Chern and spin-valley Chern numbers," Phys. Rev. B **88**, 161406 (2013).
27. S. Barik, A. Karasahin, S. Mittal, *et al.*, "Chiral quantum optics using a topological resonator," Phys. Rev. B **101**, 205303 (2020).
28. M. J. Mehrabad, A. P. Foster, R. Dost, *et al.*, "Chiral topological photonics with an embedded quantum emitter," Optica **7**, 1690 (2020).
29. Y. H. Han, H. M. Fei, H. Lin, *et al.*, "Design of broadband all-dielectric valley photonic crystals at telecommunication wavelength," Opt. Commun. **488**, 126847 (2021).
30. M. Wu, H. M. Fei, H. Lin, *et al.*, "A hexagonal boron nitride super self-collimator for optical asymmetric transmission in the visible region," Opt. Mater. **112**, 110483 (2021).
31. M. Wu, H. M. Fei, H. Lin, *et al.*, "Design of asymmetric transmission of photonic crystal heterostructure based on two-dimensional hexagonal boron nitride material," Acta Phys. Sin. **70**, 028501 (2021).
32. M. Wu, Y. B. Yang, H. M. Fei, *et al.*, "Unidirectional transmission of visible region topological edge states in hexagonal boron nitride valley photonic crystals," Opt. Express **30**, 6275 (2022).
33. M. Wu, Y. B. Yang, H. M. Fei, *et al.*, "On-chip ultra-compact hexagonal boron nitride topological ring-resonator in visible region," J. Lightwave Technol. **40**, 7610 (2022).
34. N. Chejanovsky, M. Rezai, F. Paolucci, *et al.*, "Structural attributes and photo-dynamics of visible spectrum quantum emitters in hexagonal boron nitride," Nano Lett. **16**, 7037 (2016).
35. R. Bourrellier, S. Meuret, A. Tararan, *et al.*, "Bright UV single photon emission at point defects in h-BN," Nano Lett. **16**, 4317 (2016).
36. S. Kim, J. E. Fröch, J. Christian, *et al.*, "Photonic crystal cavities from hexagonal boron nitride," Nat. Commun. **9**, 2623 (2018).
37. K. Sejeong, T. Milos, and A. Igor, "Design of photonic microcavities in hexagonal boron nitride," Beilstein J. Nanotechnol. **9**, 102 (2018).
38. H. Jiang, S. Choudhury, Z. A. Kudyshev, *et al.*, "Enhancing sensitivity to ambient refractive index with tunable few-layer graphene/hBN nanoribbons," Photonics Res. **7**, 815 (2019).
39. M. Nonahal, C. Li, H. R. Ren, *et al.*, "Engineering quantum nanophotonic components from hexagonal boron nitride," Laser Photonics Rev. **17**, 2300019 (2023).
40. M. J. Molaei, M. Younas, and M. Rezakazemi, "A comprehensive review on recent advances in two-dimensional (2D) hexagonal boron nitride," ACS Appl. Electron. Mater. **3**, 5165 (2021).
41. I. Aharonovich and M. Toth, "Quantum emitters in two dimensions," Science **358**, 170 (2017).

42. P. F. Sun, Y. Yu, Z. Y. An, *et al.*, "Deterministic time-bin entanglement between a single photon and an atomic ensemble," Phys. Rev. Lett. **128**, 060502 (2022).

43. J. K. Yang, Y. Hwang, and S. S. Oh, "Evolution of topological edge modes from honeycomb photonic crystals to triangular-lattice photonic crystals," Phys. Rev. Res. **3**, L022025 (2021).

44. R. J. Davis, Y. Zhou, D. J. Bisharat, *et al.*, "Topologically protected edge states in triangular lattices," Phys. Rev. B **106**, 165403 (2022).

45. L. Lu, J. D. Joannopoulos, and M. Soljačić, "Topological photonics," Nat. Photonics **8**, 821 (2014).

46. F. Liu and K. Wakabayashi, "Novel topological phase with a zero Berry curvature," Phys. Rev. Lett. **118**, 076803 (2017).

47. V. Varmazyari, H. Habibiyan, and H. Ghafoorifard, "Slow light in ellipse-hole photonic crystal line-defect waveguide with high normalized delay bandwidth product," J. Opt. Soc. Am. B **31**, 771 (2014).

48. J. Li, C. H. Wen, S. Gauza, *et al.*, "Refractive indices of liquid crystals for display applications," J. Disp. Technol. **1**, 51 (2005).

49. S. T. Wu, U. Efron, and L. D. Hess, "Birefringence measurements of liquid crystals," Appl. Opt. **23**, 3911 (1984).

50. W. Wang, G. Li, and D. Xue, "Study of voltage-dependent electric-control birefringence of liquid crystal," Acta Opt. Sin. **24**, 970 (2004).

51. J. L. Wang, M. Q. Du, L. L. Zhang, *et al.*, "Transmission characteristics of photonic crystal fibers based on filling different kinds of liquid crystals," Acta Phys. Sin. **64**, 120702 (2015).